

Article

Surface Damage and Microstructure Evolution of Yttria Particle-Reinforced Tungsten Plate during Transient Laser Thermal Shock

Daya Ren ¹, Ya Xi ¹, Jie Yan ², Xiang Zan ^{1,3,*} , Laima Luo ^{1,3} and Yucheng Wu ^{1,3}

¹ School of Materials Science and Engineering, Hefei University of Technology, Hefei 230009, China; hfutdaya@163.com (D.R.); xiya1995@163.com (Y.X.); luolaima@hfut.edu.cn (L.L.); ycwu@hfut.edu.cn (Y.W.)

² Anhui Heli Co., Ltd., Hefei 230601, China; yj15215695807@163.com

³ National-Local Joint Engineering Research Centre of Nonferrous Metals and Processing Technology, Hefei University of Technology, Hefei 230009, China

* Correspondence: zanx@hfut.edu.cn; Tel.: +86-551-6290-1367

Abstract: Tungsten and its alloys are considered to be the most nominated plasma-facing materials in fusion reactors, which will be exposed to enormously rigorous conditions such as thermal load, plasma exposure, and neutron radiation. At present, the research on the behavior of oxide particle-reinforced tungsten-based materials under long-term steady-state heat load and transient thermal shock is insufficient. The purpose of this study is to investigate the performance of yttria particle-reinforced tungsten plates prepared by the wet chemical method under heat loads by means of indirect coupling experiments. An Nd:YAG laser device is used to perform thermal shock events. The surface damage and microstructure evolution of rolled and fully recrystallized samples exposed to laser thermal shock are observed and analyzed. The cracking threshold of the rolled and fully recrystallized samples is about 0.40–0.48 GW/m²; the degree of surface damage of them aggravates with the increased laser power density. What is more, cracks or even melting damage could be observed on the surface and be accelerated by the process of recrystallization, resulting in the degradation of the ability to withstand the thermal shock of the material.

Keywords: tungsten; yttria; thermal shock; surface damage; microstructure



Citation: Ren, D.; Xi, Y.; Yan, J.; Zan, X.; Luo, L.; Wu, Y. Surface Damage and Microstructure Evolution of Yttria Particle-Reinforced Tungsten Plate during Transient Laser Thermal Shock. *Metals* **2022**, *12*, 686. <https://doi.org/10.3390/met12040686>

Academic Editors: Sergey N. Grigoriev and José Spinelli

Received: 22 February 2022

Accepted: 14 April 2022

Published: 16 April 2022

Publisher's Note: MDPI stays neutral with regard to jurisdictional claims in published maps and institutional affiliations.



Copyright: © 2022 by the authors. Licensee MDPI, Basel, Switzerland. This article is an open access article distributed under the terms and conditions of the Creative Commons Attribution (CC BY) license (<https://creativecommons.org/licenses/by/4.0/>).

1. Introduction

One of the biggest challenges in magnetic confinement fusion reactors is the performance of plasma-facing materials (PFMs), which are subjected to enormously rigorous conditions during service, such as thermal load, plasma exposure, and neutron radiation [1,2]. Tungsten and its alloys have an incredible advantage in high melting point (about 3410 °C), high thermal conductivity, high sputtering resistance, and low tritium retention, and are considered to be the most potential nominated materials for PFMs [3–5]. However, their applications are restricted on account of inherent shortcomings such as low-temperature brittleness, poor toughness, higher ductile-brittle transition temperature (DBTT), and lower recrystallization temperature under nuclear fusion service conditions. The heat flux of the tungsten PFMs surface can be up to 20 MW/m² during ITER steady-state heat load operation [2], leading to the degradation of material performance, such as a decrease in mechanical strength or fracture toughness, and an increase in DBTT [6,7]. In addition to the steady-state heat load, tungsten-based materials will also be exposed to transient thermal shock, causing surface roughness, cracks, recrystallization, and even melting [8,9]. Furthermore, the higher the recrystallization volume fraction and thermal shock power density, the deeper the degree of surface damage and the weaker the ability to resist transient thermal loads [9–11]. In addition, that is extremely detrimental to the continued service of tungsten materials in nuclear fusion reactors. These problems can be

tackled by alloying [12,13], fiber toughening [14,15], and particle reinforcing [16,17] with the aim of improving the comprehensive performance of tungsten-based materials. In terms of the particle reinforcement, carbide (ZrC [18,19], TiC [20,21], TaC [22]) or oxide particles (La_2O_3 [8,23], Lu_2O_3 [24], Y_2O_3 [25–27]) are introduced into the tungsten matrix to improve the mechanical properties, recrystallization temperature, and thermal shock resistance. In recent years, the rare earth oxide Y_2O_3 has been broadly applied in the second phase of strengthening of tungsten materials because of its stable chemical properties and thermal stability [25]. The yttria particles are dispersed in the tungsten matrix, which impedes the movement of grain boundaries and dislocations. Meanwhile, the dispersion-strengthened particles will produce a large number of phase interfaces and refine the grains, making the tungsten mechanical properties, recrystallization temperature, creep resistance, and radiation resistance substantially improved [4,28]. Lv et al. found that the ultra-fine grain W- Y_2O_3 composite material was capable of withstanding the thermal shock power density of 600 MW/m^2 without any cracking in the high heat load experiment, demonstrating that it had an excellent thermal shock resistance [25]. Research by Lian et al. found that W- Y_2O_3 composite material obtained by the high-energy rotary forging process had higher mechanical properties and thermal shock resistance, and the damage degree of the material increased with the increase in the thermal shock power density [17]. Kang et al. conducted a detailed study on the recrystallization kinetics of yttria particle-reinforced tungsten, finding that the introduction of Y_2O_3 particles increased the recrystallization temperature and reduced the recrystallization rate, significantly retarding the recrystallization process [29].

At present, there are no exclusive experimental facilities that can achieve the synergistic loading of steady-state heat load and transient heat load. What is more, the research on the behavior of oxide particle-reinforced tungsten-based materials under long-term steady-state heat load and transient thermal shock is insufficient. Although research on the thermal shock behavior of tungsten and its alloys has been widely reported, these studies mainly focus on the distinction between cracking threshold and crack propagation of samples obtained in different states or preparation processes under different thermal shock conditions. It is known that a small amount of damage can be tolerated. Therefore, it is necessary to study the microstructural evolution of materials in the presence of a small amount of damage. The novelty of this paper is not only to observe and analyze the surface damage of yttria particle-reinforced tungsten plate under laser thermal shock loadings but also to explore the detailed evolution of the microstructure and texture in all heat-affected zones. In the present study, laser thermal shock loadings with different power densities are applied to the yttria particle-reinforced tungsten in deformed and fully recrystallized states, aiming to explore the damage threshold and the influence of the yttria particles on crack propagation. The microstructure evolution of the tungsten matrix and the redistribution of yttria particles after melting will be discussed.

2. Materials and Experiment

W- Y_2O_3 composite powder is obtained by wet chemical method. The powder was prepared from the nitrate of Y_2O_3 ($\text{Y}(\text{NO}_3)_3 \cdot 6\text{H}_2\text{O}$) and ammonium paratungstate ($(\text{NH}_4)_6\text{H}_2\text{W}_{12}\text{O}_{40} \cdot x\text{H}_2\text{O}$). Oxalic acid ($\text{C}_2\text{H}_2\text{O}_4 \cdot 2\text{H}_2\text{O}$) served as the precipitating agent aimed at the preparation of precursor. Then put the precursor powder into the continuous reduction furnace after evaporating precipitation. Next, W- Y_2O_3 composite powder was condensed by cold isostatic pressing and sintered in a hydrogen atmosphere furnace at $2300 \text{ }^\circ\text{C}$ for 6 h to obtain sintered billet, which was warm-rolled to a thickness reduction of 50% at Beijing Tian-Long Tungsten & Molybdenum Co., Ltd, Beijing, China. (W-2 vol% Y_2O_3 , abbreviated as WY50). The ratio of the 2 vol% Y_2O_3 dopant was calculated using the stoichiometry of $\text{Y}(\text{NO}_3)_3 \cdot 6\text{H}_2\text{O}$. The size of Y_2O_3 particles ranged from $0.5 \text{ }\mu\text{m}$ to $2.1 \text{ }\mu\text{m}$, uniformly distributed in the tungsten matrix. After rolling, an isothermal annealing treatment at $1000 \text{ }^\circ\text{C}$ was carried out for 2 h to eliminate stress [29]. Small specimens of $10 \times 10 \times 3 \text{ mm}^3$ were cut from the rolled plate along rolling direction (RD) \times normal direction (ND) \times transverse direction (TD) by electrical discharge wire cutting. The high-temperature heat treatment experiment was required to obtain recrystallized samples. The specimens were sealed in a vacuum quartz tube to prevent

the oxidation of tungsten before heat treatment. After that, an isothermal annealing experiment at 1300 °C was performed for 42 h in a muffle furnace to obtain fully recrystallized samples in accordance with the hardness evolution curve of the recrystallization kinetics process obtained in the previous study [29].

The surface of all samples was ground with SiC papers and mechanical polished with diamond paste, subsequently corroded with boiling H₂O₂ aqueous solution (H₂O: 30% H₂O₂ = 2:1) about 50 s for metallographic and 3D laser confocal microstructure observation.

Then, laser thermal shock experiment was conducted on the RD–ND surface of rolled and fully recrystallized samples. The set-up and parameters are shown in Table 1.

Table 1. The parameters of laser thermal shock experiment.

Parameter/(Unit)	Values				
Frequency/(Hz)	15				
Laser point diameter/(mm)	0.6				
Irradiation time/(ms)	2				
Flow rate of H ₂ /(L·min ^{−1})	10				
Current/(A)	60	75	90	105	120
Power density/(GW·m ^{−2})	0.32	0.40	0.48	0.56	0.64

Three-dimensional confocal laser scanning microscope (CLSM, VK-X1000, Keyence, Osaka, Japan) was utilized to observe the surface morphologies of the thermal shock samples and the surface damage parameters were statistically analyzed by the Multi File Analyzer software equipped by CLSM.

Electron backscatter diffraction (EBSD) was used to accurately characterize the microstructure of samples. For EBSD investigations, the surfaces of all the samples were mechanically ground with silicon carbide paper and polished with 2.5 μm and 0.5 μm diamond polishing paste, then finishing polished with 0.04 μm OP-U non-drying suspension produced by Struers. Finally, the samples were additionally electropolished with 3 wt% NaOH aqueous solution at a constant voltage of 8 V about 15 s. EBSD testing was conducted by a scanning electron microscope (SEM, ZEISS Gemini 500, Carl Zeiss AG, Oberkochen, Germany) with an Oxford C-Swift detector (Oxford Instruments, Oxford, UK) using a voltage of 20 kV with a step size of 1 μm.

3. Results and Discussion

3.1. Initial Samples before Thermal Shock

The initial microstructure of the RD–ND surface and TD–ND surface of the rolled and fully recrystallized samples is presented in Figure 1. The grains on the RD–ND surface of the rolled sample are elongated along the rolling direction (Figure 1a). After full recrystallization, the microstructures of the two sections change significantly, and the original deformed grains are replaced by the equiaxed grains.

Figure 2 shows the grain boundary and misorientation distribution figures of the TD–ND surface of the rolled and fully recrystallized samples. The solid green line is a low-angle grain boundary with a misorientation angle of between 2° and 15°, and the black line is a high-angle grain boundary with a misorientation angle of more than 15°. The rolled sample has the typical characteristic of a deformed structure with a large number of low-angle grain boundaries inside the grains. As for the fully recrystallized sample, it is mainly composed of undistorted equiaxed grains, whose misorientation distribution is closer to the Mackenzie distribution baseline.

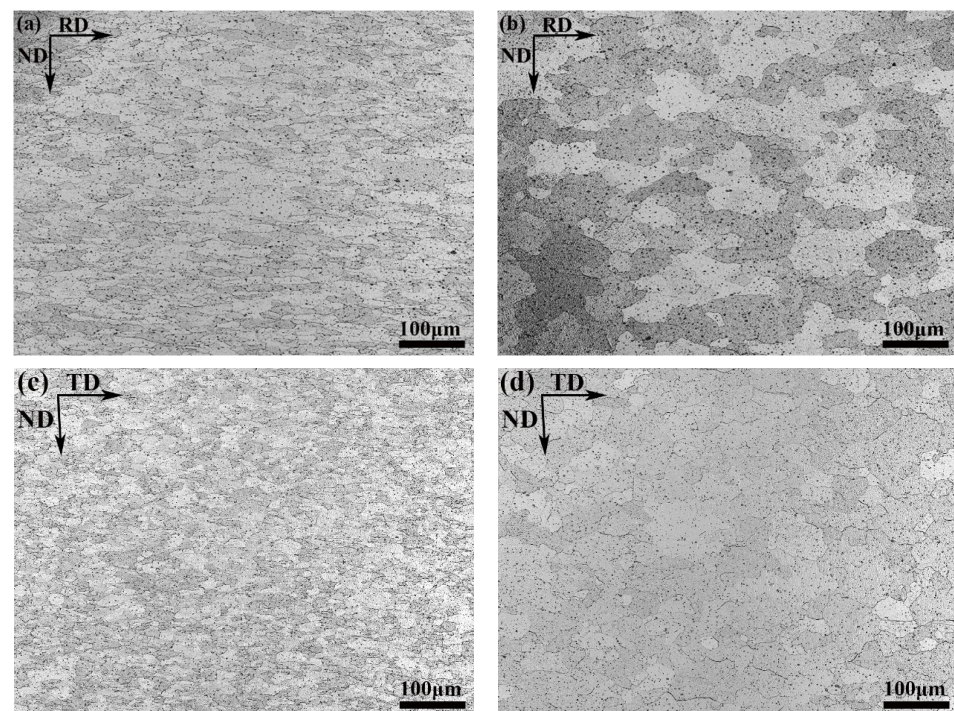


Figure 1. Microstructure of WY50 plate: rolled sample (a,c) and fully recrystallized sample (b,d).

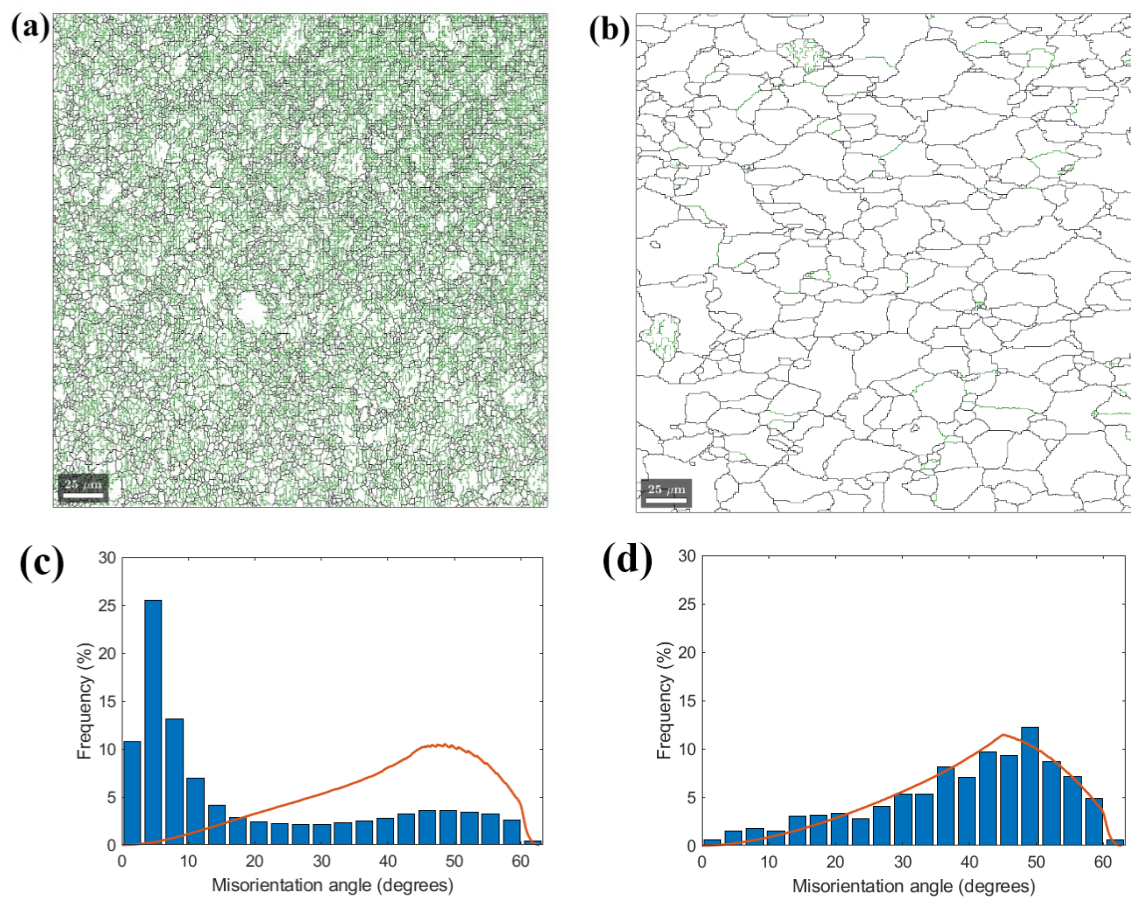


Figure 2. Grain boundary maps (top) and orientation distribution maps (bottom) of the TD–ND surface of the rolled sample (a,c) and fully recrystallized sample (b,d).

The orientation maps and inverse pole figures (IPF) of the rolled and fully recrystallized sample with a TD–ND surface are shown in Figure 3. The rolled sample mainly consisted of grains with $\langle 110 \rangle // \text{RD}$ and $\langle 111 \rangle // \text{ND}$. After complete recrystallization, the intensity of $\langle 110 \rangle // \text{RD}$ is weakened, while there is almost no obvious change in the intensity of $\langle 111 \rangle // \text{ND}$.

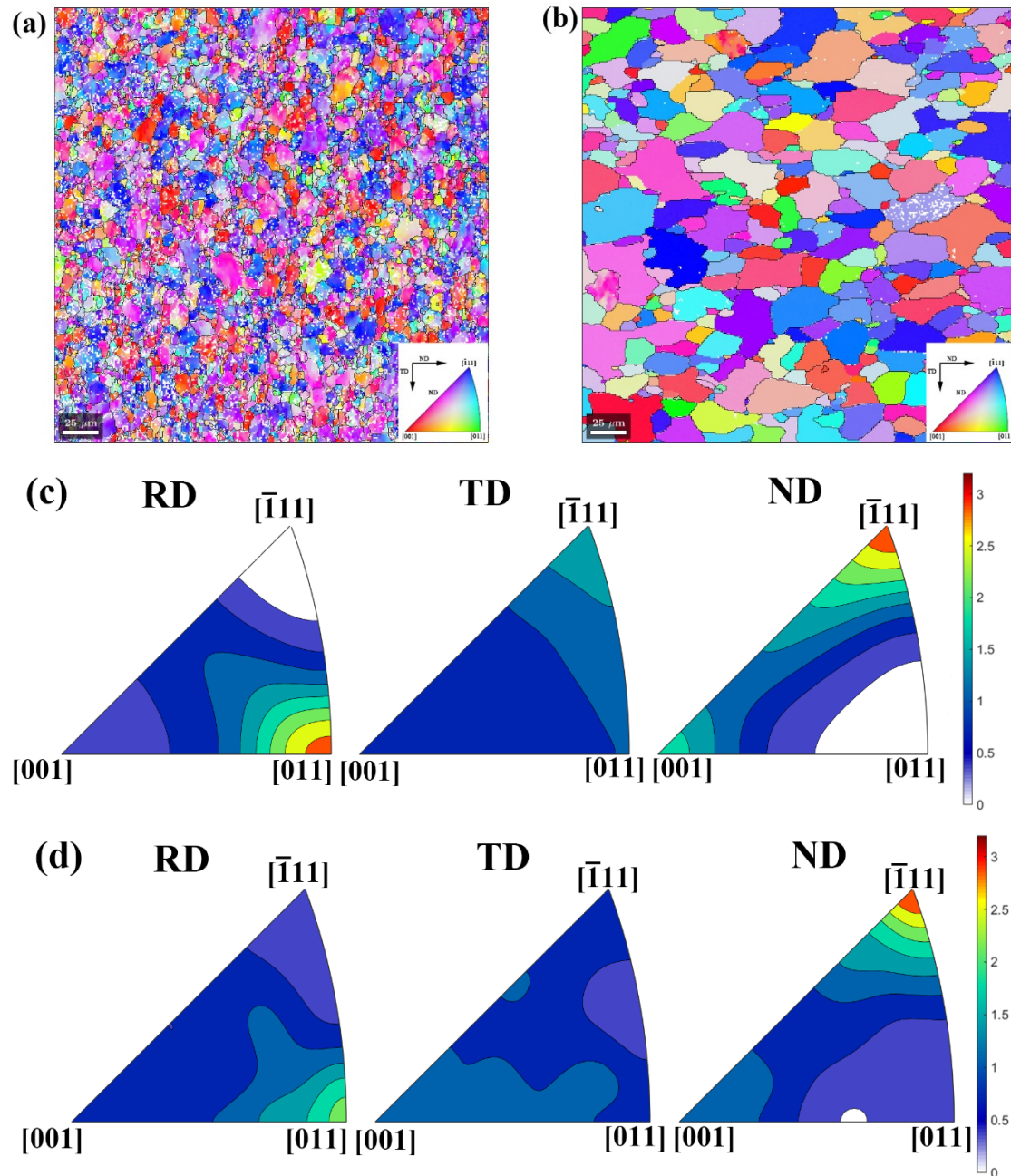


Figure 3. Orientation maps (top) and IPFs (bottom) of the TD–ND surface of the rolled sample (a,c) and fully recrystallized sample (b,d).

Figure 4 gives the orientation distribution functions (ODFs) of $\varphi_2 = 45^\circ$ for the rolled and fully recrystallized sample, showing that the typical texture of the rolled sample with a body-centered cube structure is mainly composed of the following three fiber texture components: α -fiber with $\{112\} \langle 110 \rangle$ components, γ -fiber with $\{111\} \langle 112 \rangle$, $\{111\} \langle 110 \rangle$ components, and a weaker θ -fiber. The textures of samples with α -fiber and θ -

fiber disappeared and degenerated, but they still maintained a strong γ -fiber texture after complete recrystallization.

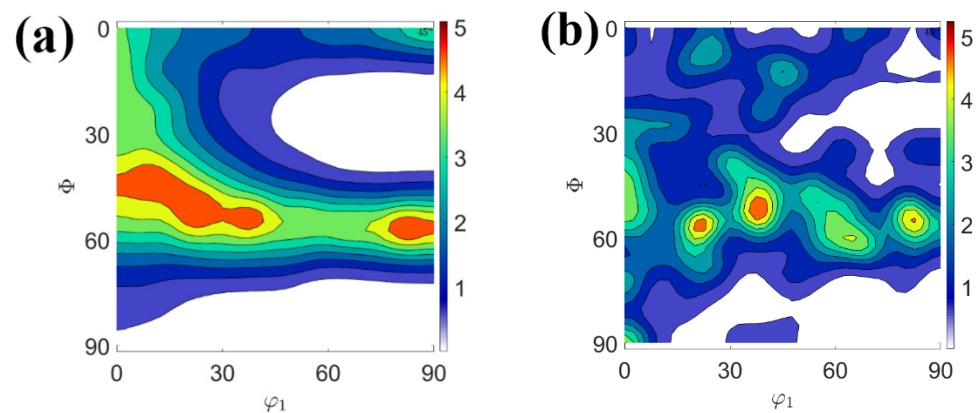


Figure 4. The ODFs of the rolled sample (a) and fully recrystallized sample (b).

3.2. The Samples after Thermal Shock

Figure 5 presents the surface morphologies in the center affected area of the rolled and fully recrystallized samples with different thermal shock power densities. There is no obvious crack damage or melting on the surface of all samples when the power density is 0.32 GW/m^2 . A crack parallel to the horizontal direction along the RD direction is found on the surface of all samples at a power density of 0.40 GW/m^2 , which is higher than that of pure tungsten [30]. The thermal tensile stress is caused by the temperature gradient perpendicular to the heated surface during the heating process, when the tensile stress exceeds the tensile strength of W- Y_2O_3 materials, cracks will occur [31]. The grains are elongated along the rolling direction, and the grain boundaries are parallel to the RD direction. While the cracks in the ND direction are longitudinal, the cracks will propagate along the grain boundaries under the thermal shock, so the cracks parallel to the RD direction will be observed on the surface [32,33]. It can be observed that melting has emerged to appear on the thermal shock surface of all samples apart from cracks under the power density of 0.48 GW/m^2 . When the power density increases to 0.64 GW/m^2 , the degree of melting aggravates, and the shape of the molten area is different from that of the fully recrystallized sample, which is closer to a circle.

Figure 6 exhibits the local surface morphologies from Figure 5 of thermal shock samples. Only one crack along the rolling direction appears on the surface of the rolled sample at a power density of 0.40 GW/m^2 , while the cracks along the RD direction begin to bifurcate, and secondary cracks can be observed on the surface of the fully recrystallized sample. The propagation direction of the crack may be changed and even hindered by the yttria particles. What is more, the grain-bonding strength will be reduced after recrystallization, which leads to the appearance of microcracks on the surface of the fully recrystallized sample [34]. There is no obvious difference in the molten zone and cracking behavior between the rolled and fully recrystallized samples under the higher power density.

Figure 7 shows the 3D height color map of the fully recrystallized samples under laser thermal shock with different power densities, observing that the higher the power density, the more apparent the fluctuation of the surface. As shown in the heightmap, a bulge formed in the center of the molten zone with the increased power density. Under the circumstances of higher thermal shock power density, the heat-loading region of the sample melts. Then, a molten pool is generated, and the edge of it rises because of surface tension. Next, molten tungsten converges from the edge to the center because of counteracting force and starts to fluctuate. Finally, after laser thermal shock, molten W solidifies as it gathers from the edge to the center [35,36]. Figure 8 presents the variation of the maximum and minimum height values of the thermal shock surface with the increased power density, showing that the power density of 0.40 GW/m^2 is a dividing line. The highest and lowest

heights of the surface of the sample remain stable below the power density of 0.40 GW/m^2 , while the height of the surface is varied drastically owing to the melting of the sample when the power density is increased. The higher the power density, the higher the temperature on the surface, and the lower the viscosity of molten tungsten and yttria; therefore, they are likely to flow, and the fluctuation is more intense under the action of thermal shock.

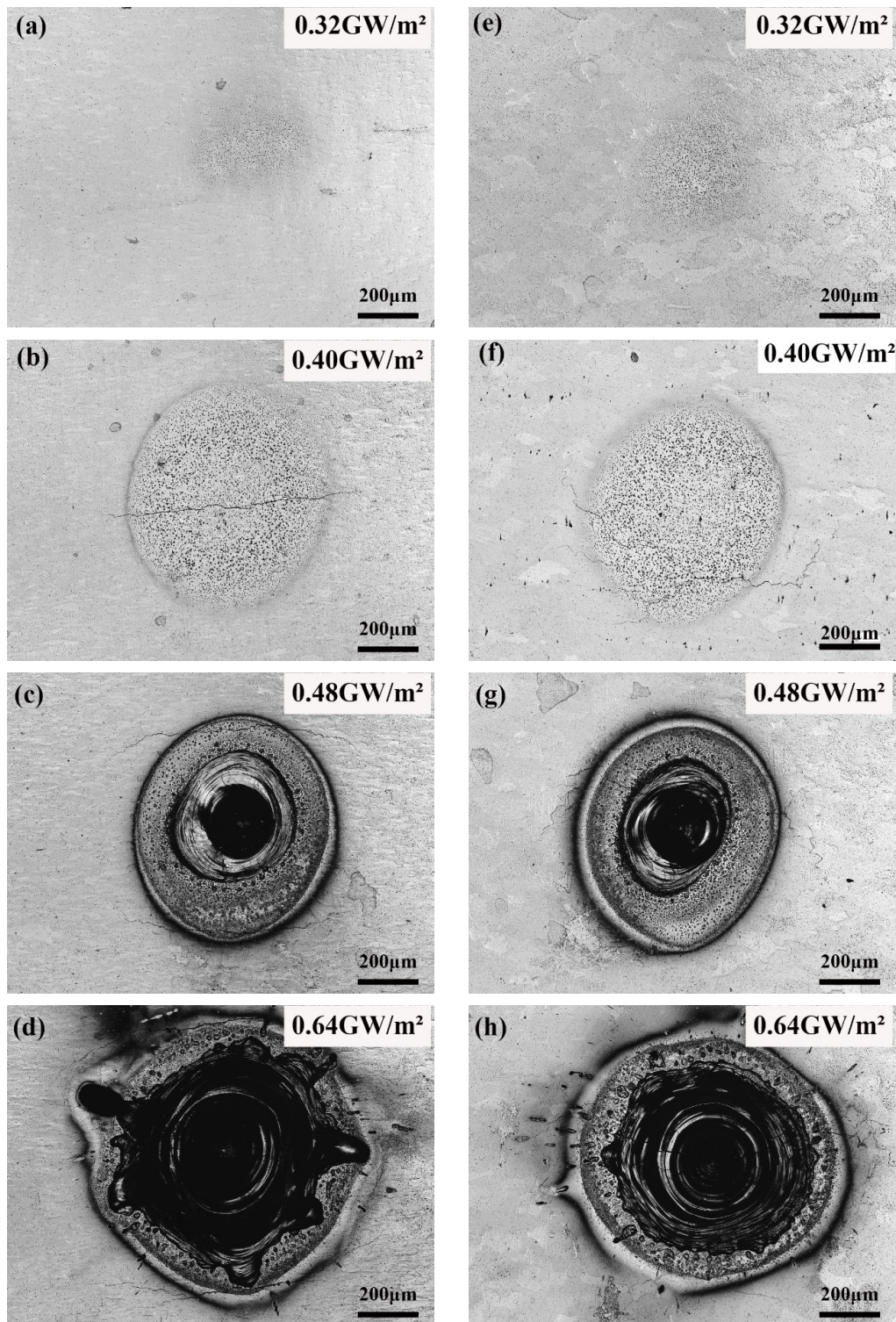


Figure 5. Surface morphologies of WY50 samples under different laser thermal shock power densities: rolled samples (a–d); fully recrystallized samples (e–h).

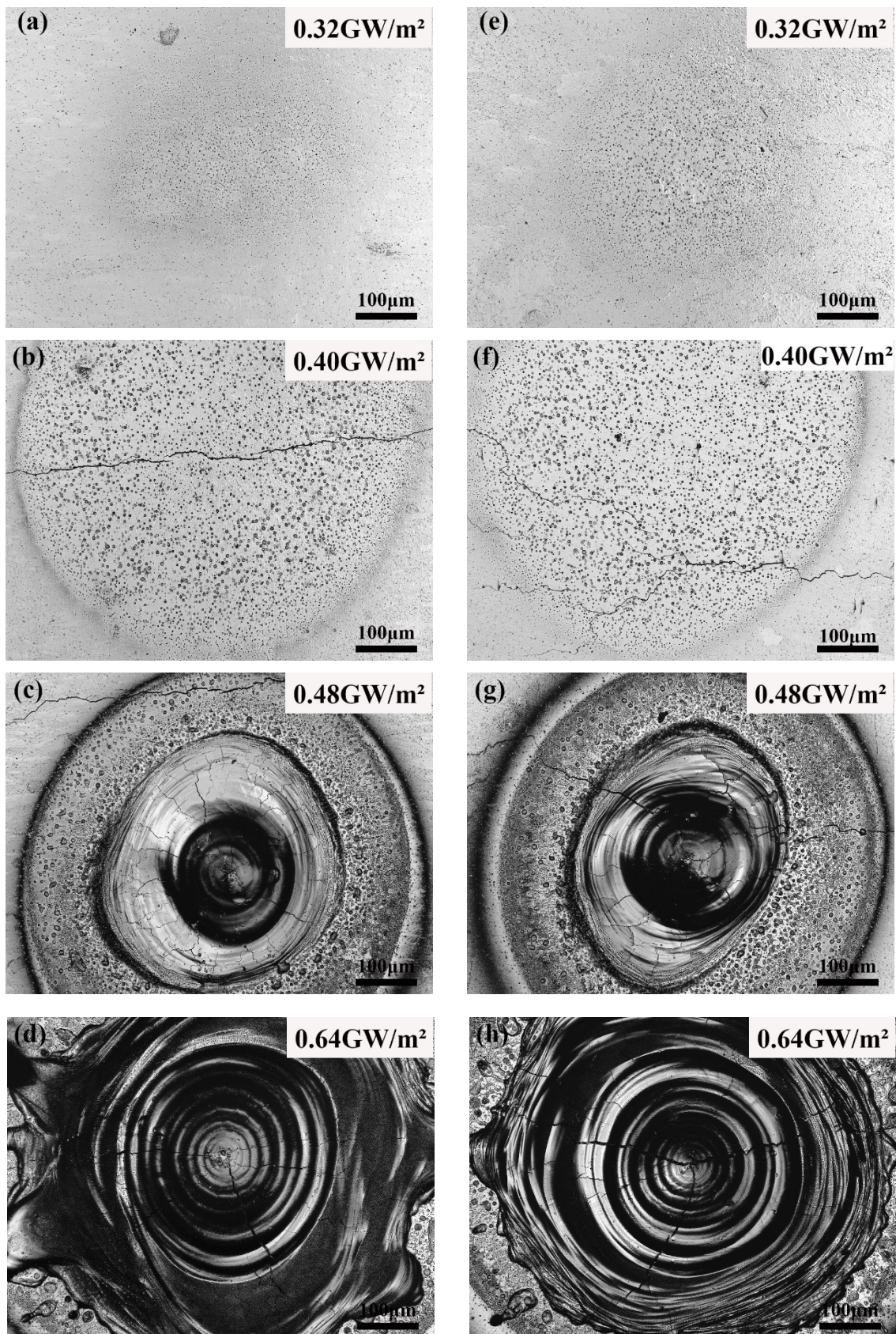


Figure 6. The local surface morphologies corresponding to the Figure 5 (a–h): rolled samples (a–d); fully recrystallized samples (e–h).

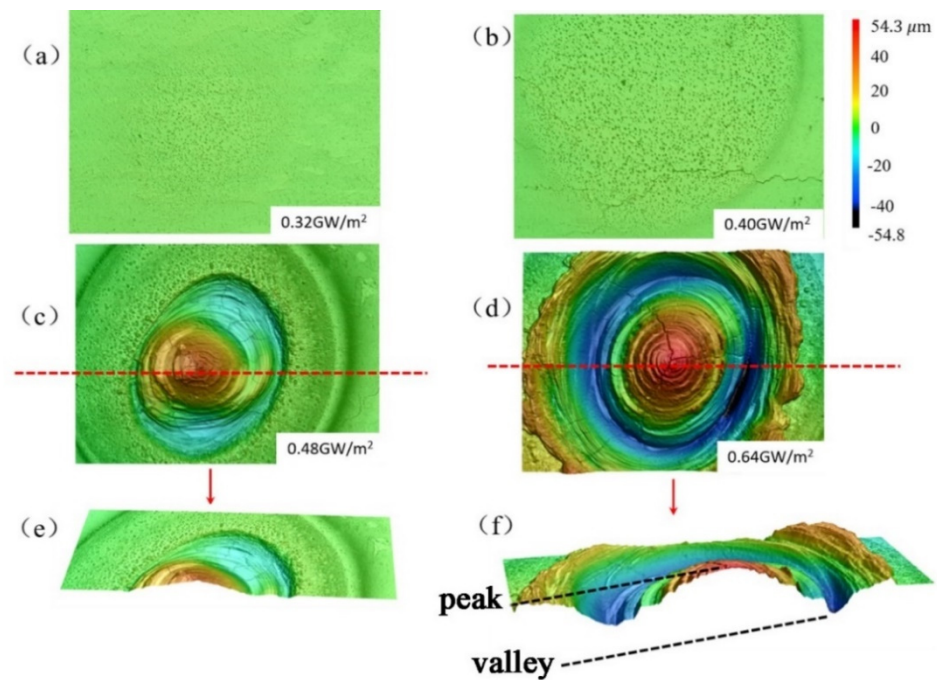


Figure 7. The 3D height color maps of the fully recrystallized samples under laser thermal shock with different power densities: (a) 0.32 GW/m²; (b) 0.40 GW/m²; (c) 0.48 GW/m²; (d) 0.64 GW/m²; (e) the sectional image of (c) along the red dotted line; (f) the sectional image of (d) along the red dotted line.

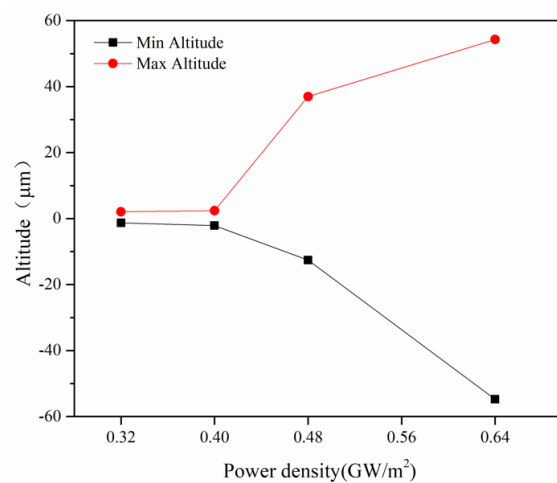


Figure 8. The variation of the maximum height value and the minimum height value of the fully recrystallized samples with the power density.

The schematic diagram of the damage with different power densities is shown in Figure 9. It reveals that the thermal shock surface can be classified into three zones at higher power densities, namely, the molten zone (I), the heat-affected zone (HAZ, II), and the unaffected zone (III). Figure 10 represents the SEM images of the surface morphologies of the fully recrystallized sample at a power density of 0.64 GW/m². Under the effect of laser power impact, tungsten and yttria particles melt. Yttria particles may gather and solidify owing to the fluctuation, eventually possibly being pushed into the HAZ because of its lower density than W. Part of them flows back to the molten zone under the flow action of metal liquid in the HAZ, ultimately forming the larger yttria particles in the molten zone after solidification. The pressure above the exposed surface from the evaporated material generates a pressure gradient, which causes liquid material movement mainly along the radial direction, resulting in the formation of a ridge around the periphery of the irradiated

spot. A possible mechanism of liquid droplet splashing was Kelvin–Helmholtz instability and boiling of superheated liquid as a result of the reduction in vapor pressure [37]. Similar splashing of liquid droplets has been reported from the tungsten surface at a heat load higher than the melting threshold with a plasma gun [38].

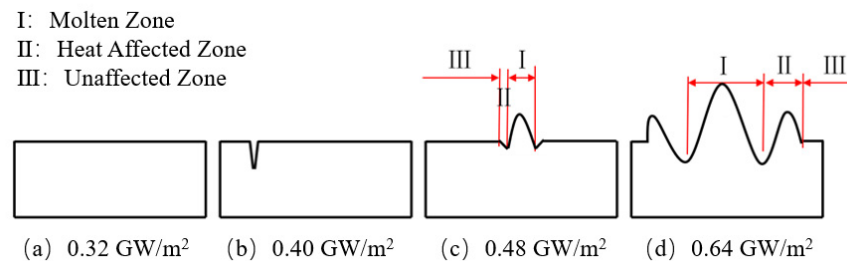


Figure 9. The schematic diagram of the damage with different power densities: (a) 0.32 GW/m²; (b) 0.40 GW/m²; (c) 0.48 GW/m²; (d) 0.64 GW/m².

I: Molten Zone;

II: Heat Affected Zone;

III: Unaffected Zone

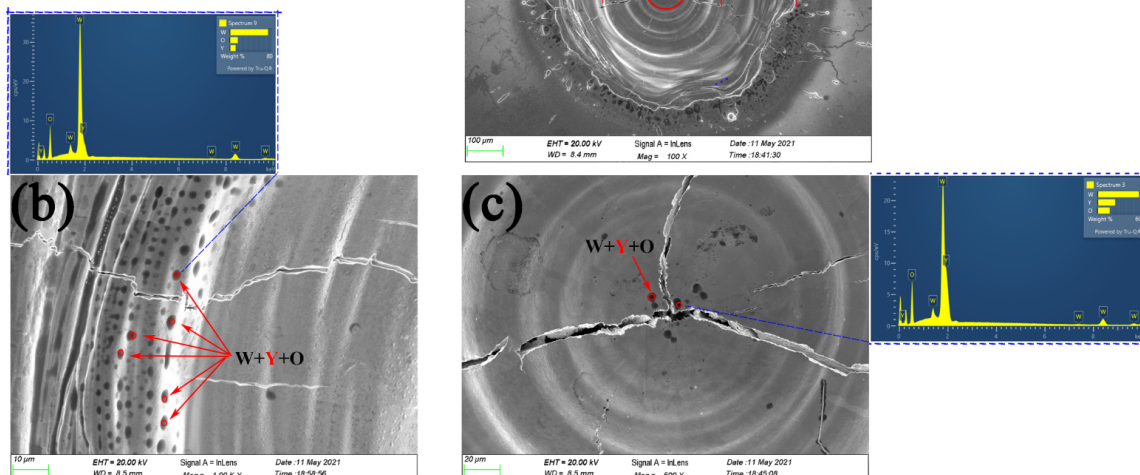


Figure 10. SEM images of the fully recrystallized sample at 0.64 GW/m²: (a) the heat loading zone; (b) the HAZ; (c) the molten zone.

Figure 11 demonstrates the surface morphologies of the molten zone at the center of the surface under the power density between 0.48 and 0.64 GW/m². In the case of the same recrystallization volume fraction, numerous and finer cracks are observed at a power density of 0.48 GW/m², and the width of cracks remarkably increases with the increased power density. When the power density is constant, the crack width of the fully recrystallized samples is larger than that of the rolled samples under a high power density (Figure 11c,d), demonstrating that the thermal shock resistance of the material degrades with the increase in the recrystallization volume fraction. In the recrystallization process, some impurities may be enriched in the grain boundary. The surface energy will be reduced with the increased recrystallization. The stress would be concentrated on the grain boundary under the heat loading, accelerating the propagation of cracks [39].

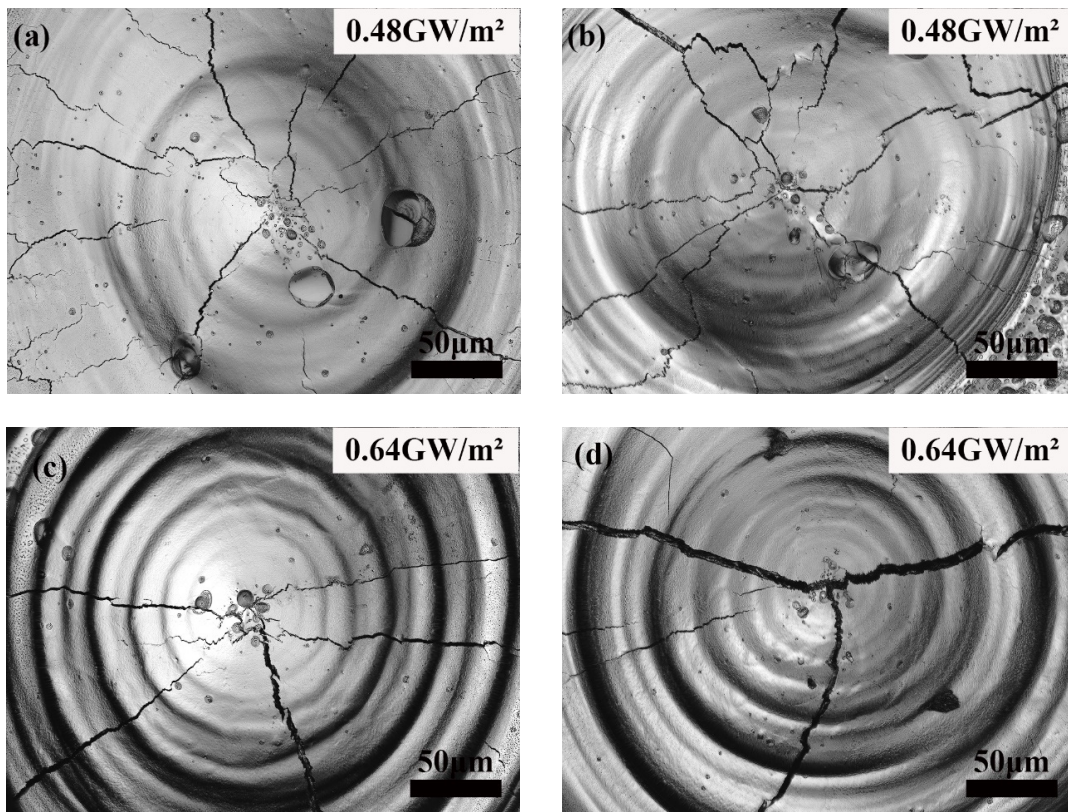


Figure 11. The local surface morphologies from Figure 6c,d,g,h: rolled sample (a,c) and fully recrystallized sample (b,d).

Figure 12 illustrates the distribution of surface damage characteristics of the rolled and fully recrystallized samples under laser thermal shock with different power densities. There is no apparent damage on the surface when the power density is less than 0.40 GW/m^2 ; cracks can be observed on the surface, and recrystallization has a great influence on the crack propagation of the material when the power density exceeds 0.40 GW/m^2 ; the surface of the samples melts when it is more than 0.48 GW/m^2 . The higher the power density, the more severe the damage. The higher the power density, the higher the surface temperature and the heat flux, which will cause a stronger thermal impact and increase severe damage [40].

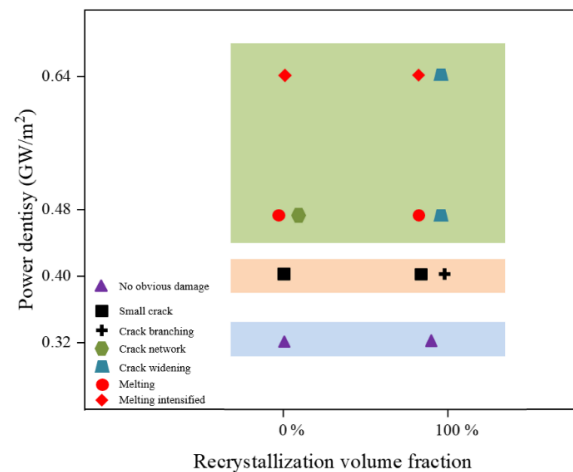


Figure 12. The distribution of surface damage characteristics of the rolled and fully recrystallized samples under laser thermal shock with different power densities.

The average crack width on the surface calculated from Figure 11 is shown in Figure 13, indicating that the average crack width with power density increases overall, but there is an abnormality that the average crack width decreases when the power density increases from 0.40 to 0.48 GW/m^2 . The reason for the above result is that the sample melts first and forms a molten pool on the surface under the high laser thermal shock power density. Then the molten sample solidifies and releases most of the thermal stress after the laser thermal shock, forming the wider cracks in the molten zone [36]. The average crack width of the fully recrystallized samples is wider than that of the rolled samples all the time, no matter what the power density is. Furthermore, the average crack width on the surface of the fully recrystallized samples increases sharply with the increased power density, revealing that the ability of the material to resist laser thermal shock is prominently degenerated because of recrystallization.

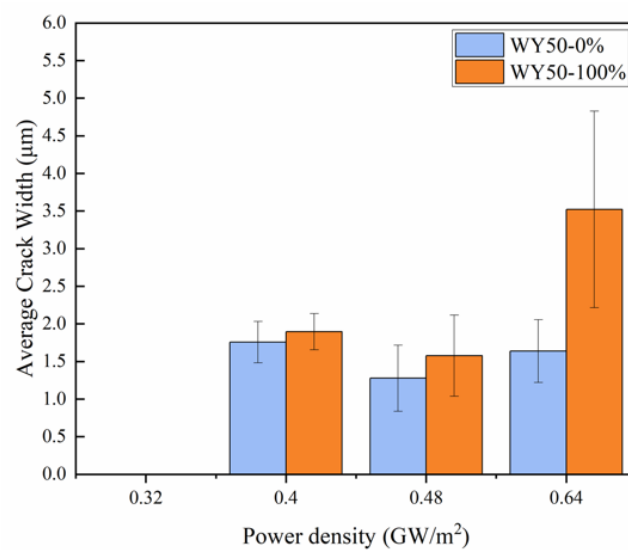


Figure 13. The average crack width variation of WY50 sample with different power densities.

Figure 14 shows the microstructure of the TD–ND surface of the rolled and fully recrystallized sample at a power density of 0.40 GW/m^2 after electropolishing. The recrystallized sample has a deeper crack depth than the rolled sample, about 86.855 μm deeper, which indicates that the ability of the material to resist thermal shock declines after recrystallization.

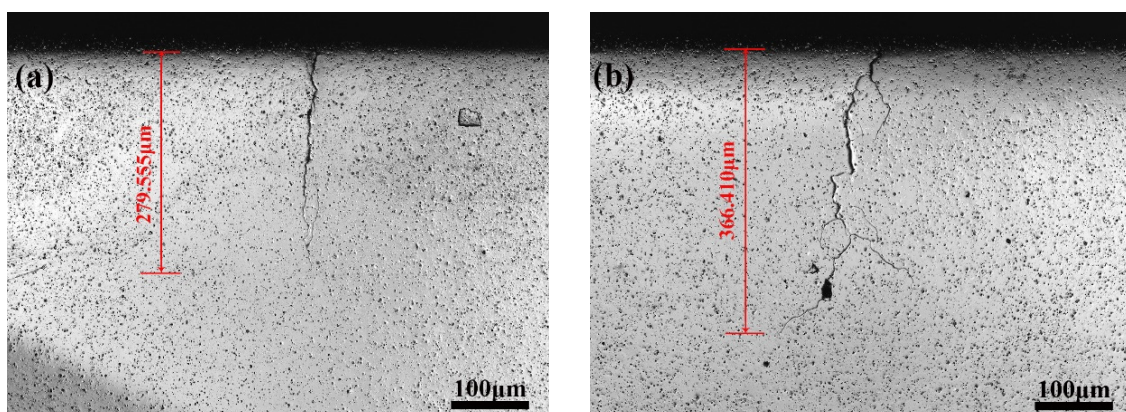


Figure 14. The 3D confocal microstructure of the TD–ND surface at the power density of 0.40 GW/m^2 : the rolled sample (a); fully recrystallized sample (b).

Figure 15 shows the 3D confocal microstructure of the rolled and fully recrystallized sample at a power density of 0.64 GW/m^2 , whose thermal shock surface (RD–ND surface) and corresponding cross-section (TD–ND surface) are represented by height color image and laser image, respectively. The molten zone (I) and the HAZ (II), as shown in Figure 9 (zone III cannot be observed in the magnification of Figure 15) in the cross-section, can be marked by the heightmap above. What is more, the crack propagation manner at this power density is the same as that at a power density of 0.40 GW/m^2 .

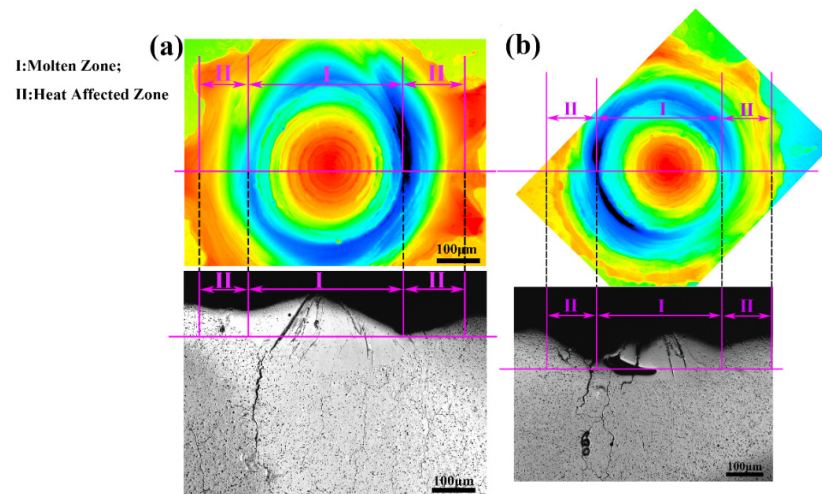


Figure 15. The 3D confocal microstructure of the thermal shock surface (RD–ND surface) and the cross-section (TD–ND surface) at the power density of 0.64 GW/m^2 : the rolled samples (a) and fully recrystallized samples (b).

Figure 16 displays the microstructure of the TD–ND surface of the rolled and fully recrystallized samples at 0.64 GW/m^2 , finding that the molten zone is the columnar zone and the cracks in the zone are intergranular fractures from the backscattering electron (BSE) image and the orientation map. What is more, the width of the columnar grains is associated with the grain size of the initial matrix below. The columnar grains formed in rolled samples are finer and more numerous, while those of the fully recrystallized samples are coarser.

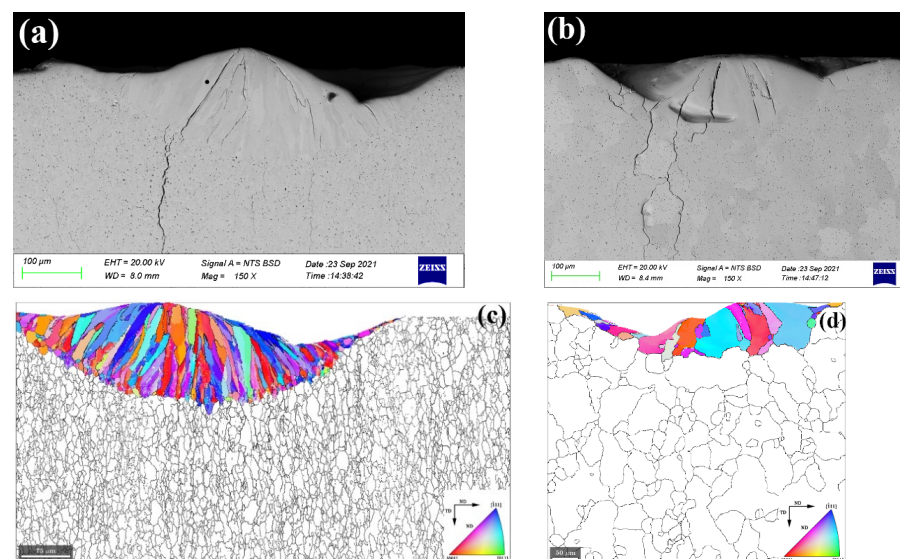


Figure 16. The BSE image (top) and orientation map (bottom) of the TD–ND surface of the rolled samples (a,c) and fully recrystallized samples (b,d) at 0.64 GW/m^2 .

Figure 17 represents the IPFs and ODFs of the molten zone of the rolled and fully recrystallized samples at 0.64 GW/m^2 . The molten zone of the rolled sample was not only composed of grains with $\langle 111 \rangle // \text{ND}$ and $\langle 110 \rangle // \text{RD}$ but also consisted of grains with $\langle 100 \rangle // \text{ND}$, compared with the initial rolled sample (Figure 3c,d). After fully recrystallization, the intensity of the grains with $\langle 110 \rangle // \text{RD}$ is significantly enhanced, while that of $\langle 100 \rangle // \text{ND}$ is evidently weakened, arising stronger grains with an orientation of $\langle 332 \rangle // \text{ND}$ and $\langle 411 \rangle // \text{TD}$. From the ODFs, the texture of the molten zone of the rolled sample is mainly composed of θ -fiber and γ -fiber with a component of $\{111\} \langle 112 \rangle$. After full recrystallization, only γ -fiber with a higher strength component of $\{111\} \langle 110 \rangle$ exists in the molten zone, and the θ -fiber is completely degraded.

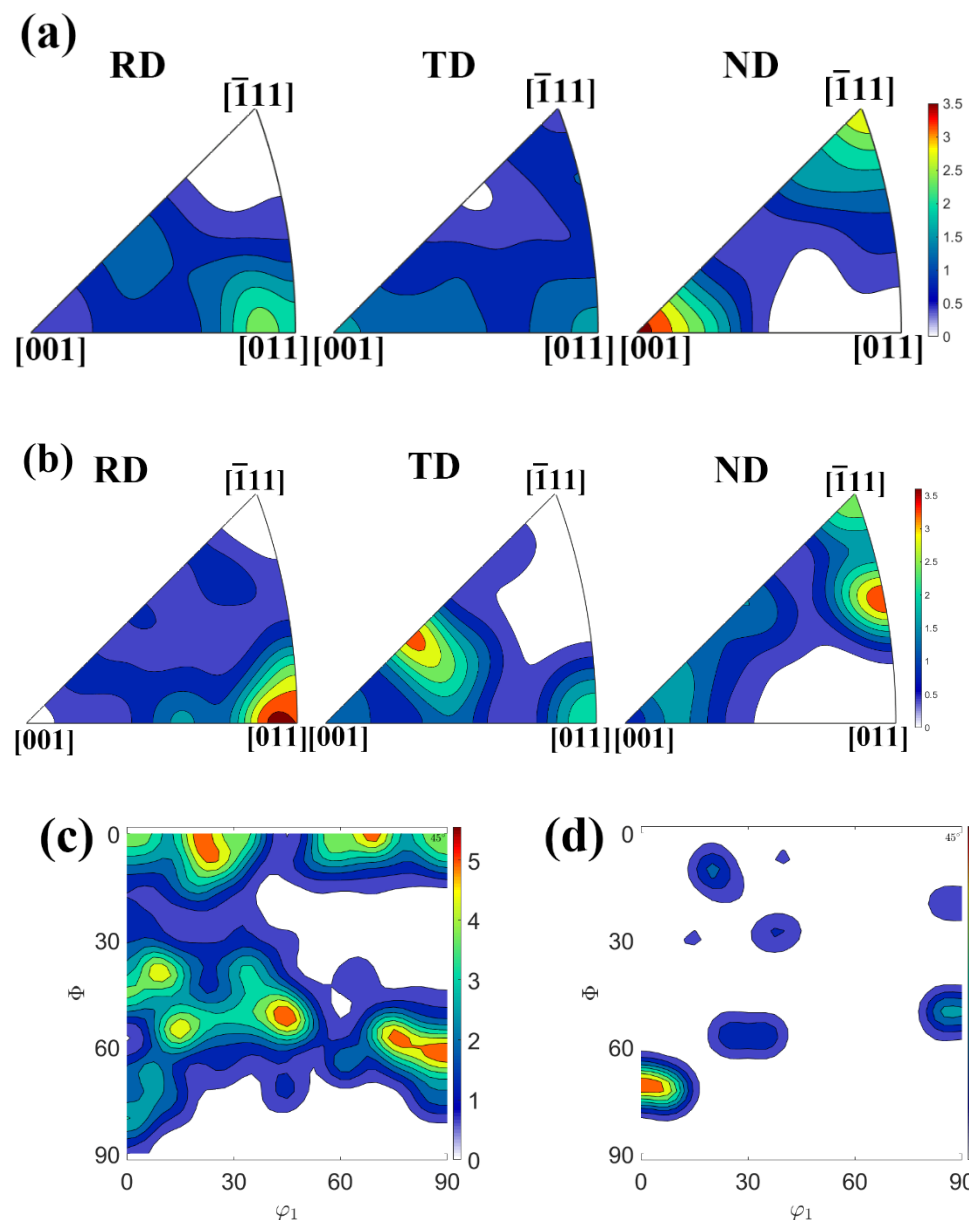


Figure 17. The IPFs (top) and ODFs (bottom) of the molten zone of the rolled sample (a,c) and fully recrystallized samples (b,d) at 0.64 GW/m^2 .

4. Conclusions

The surface damage morphologies and the microstructure evolution of the rolled and fully recrystallized $\text{W-Y}_2\text{O}_3$ samples subjected to the transient laser heat load with different power densities have been investigated. The following conclusions can be drawn:

- (1) The cracking threshold of the rolled and fully recrystallized samples is about 0.40–0.48 GW/m². The degree of surface damage of the samples aggravates with the increased laser power density. What is more, cracking, or even melting damage, could be observed on the surface and be accelerated by the process of recrystallization, resulting in the degradation of the ability to withstand the thermal shock of the material;
- (2) The average crack width with power density increases overall, but there is an abnormality that the average crack width decreases when the power density increases from 0.40 to 0.48 GW/m². In addition, the average crack width of the fully recrystallized sample is always wider than that of the rolled sample, no matter what the power density is. Furthermore, the average crack width on the surface of the fully recrystallized sample increases sharply with the increased power density;
- (3) Yttria particles have the ability to inhibit crack propagation to a certain extent at low-power densities. In the case of high-power densities, the heat-loading region melted, and most of the Yttria particles were pushed into the HAZ, contributing to the fewer particles and coarser cracks in the molten zone;
- (4) Plenty of columnar grains appear in the molten zone, and the cracks in the zone are intergranular fractures at a power density of 0.64 GW/m². What is more, the width of the columnar grains is closely associated with the grain size of the initial material. The columnar grains formed in the rolled samples are finer and more numerous, mainly consisting of grains with the orientation of <100> // ND, <111> // ND, and <110> // RD. On the contrary, the columnar grains formed in the fully recrystallized samples are coarser. The grains with an orientation of <110> // RD and <100> // ND are significantly enhanced and weakened, respectively, generating the new grains with an orientation of <332> // ND and <411> // TD.

Author Contributions: Conceptualization, D.R. and X.Z.; methodology, D.R. and X.Z.; validation, X.Z., L.L. and Y.W.; investigation, D.R., Y.X. and J.Y.; resources, L.L.; data curation, D.R.; writing—original draft preparation, D.R.; writing—review and editing, D.R. and X.Z.; supervision, X.Z. and Y.W.; project administration, L.L. and Y.W.; funding acquisition, Y.W. All authors have read and agreed to the published version of the manuscript.

Funding: This work was supported by the National MCF Energy R&D Program (2019YFE03120003).

Data Availability Statement: Data sharing is not applicable.

Acknowledgments: The authors would like to acknowledge the financial support from the National MCF Energy R&D Program (2019YFE03120003).

Conflicts of Interest: The authors declare no conflict of interest.

References

1. Linsmeier, C.; Rieth, M.; Aktaa, J.; Chikada, T.; Hoffmann, A.; Hoffmann, J.; Houben, A.; Kurishita, H.; Jin, X.; Li, M.; et al. Development of advanced high heat flux and plasma-facing materials. *Nucl. Fusion*. **2017**, *57*, 092007. [[CrossRef](#)]
2. Linke, J.; Du, J.; Loewenhoff, T.; Pintsuk, G.; Spilker, B.; Steudel, I.; Wirtz, M. Challenges for plasma-facing components in nuclear fusion. *Matter Radiat. Extrem.* **2019**, *4*, 056201. [[CrossRef](#)]
3. Han, X.Y.; Liu, X.L.; Wang, D.Z.; Wu, Z.Z.; Duan, B.H. Copper-based tungsten coating by CVD: Microstructure, thermal shock resistance and interfacial bond force. *Surf. Coat. Tech.* **2021**, *426*, 127778. [[CrossRef](#)]
4. Yao, G.; Chen, H.Y.; Zhao, Z.H.; Luo, L.M.; Ma, Y.; Cheng, J.G.; Zan, X.; Xu, Q.; Wu, Y.C. The superior thermal stability and irradiation resistance capacities of tungsten composites synthesized by simple second-phase particle component modulation. *J. Nucl. Mater.* **2022**, *561*, 153522. [[CrossRef](#)]
5. Koike, A.; Yamazaki, S.; Wada, T.; Sun, F.; Yoshida, N.; Hanada, K.; Oya, Y. Evaluation of hydrogen retention behavior for damaged tungsten exposed to hydrogen plasma at QUEST with high temperature wall. *Fusion Eng. Des.* **2022**, *176*, 113020. [[CrossRef](#)]
6. Guan, W.; Nogami, S.; Fukuda, M.; Sakata, A.; Hasegawa, A. Effect of Grain Structure Anisotropy and Recrystallization on Tensile Properties of Swaged Tungsten Rod. *Plasma Fusion Res.* **2017**, *10*, 1405073. [[CrossRef](#)]
7. Wang, K.; Ren, D.Y.; Zan, X.; Luo, L.M.; Zhu, X.Y.; Wu, Y.C. Recrystallization behavior of pure tungsten hot-rolled with high accumulated strain during annealing at 1250 °C–1350 °C. *Mater. Sci. Eng. A-Struct.* **2021**, *806*, 140828. [[CrossRef](#)]

8. Zhang, X.X.; Gong, Z.; Huang, J.J.; Yu, B. Thermal shock resistance of tungsten with various deformation degrees under transient high heat flux. *Mater. Res. Express*. **2020**, *7*, 066503. [[CrossRef](#)]
9. Zan, X.; Yan, J.; Sun, H.T.; Wang, K.; Lian, Y.Y.; Tan, X.Y.; Luo, L.M.; Liu, X.; Wu, X.C. Surface damage during transient thermal load of 50% thickness reduced W-2% (Vol.) Y₂O₃ sheet with different recrystallization volume fraction. *Int. J. Refract. Met. Hard Mater*. **2020**, *88*, 105197. [[CrossRef](#)]
10. Huber, A.; Arakcheev, A.; Sergienko, G.; Steudel, I.; Wirtz, M.; Burdakov, A.V.; Coenen, J.W.; Kreter, A.; Linke, J.; Mertens, P.; et al. Investigation of the impact of transient heat loads applied by laser irradiation on ITER-grade tungsten. *Phys. Scr*. **2014**, *T159*, 014005. [[CrossRef](#)]
11. Suslova, A.; El-Atwani, O.; Sagapuram, D.; Hassanein, A. Recrystallization and grain growth induced by ELMs-like transient heat loads in deformed tungsten samples. *Sci. Rep*. **2014**, *4*, 6845. [[CrossRef](#)] [[PubMed](#)]
12. Kurishita, H.; Matsuo, S.; Arakawa, H.; Kobayashi, S.; Nakai, K.; Takida, T.; Takebe, K.; Kawai, M. Superplastic deformation in W-0.5 wt.% TiC with approximately 0.1 μ m grain size. *Mat. Sci. Eng. A-Struct*. **2008**, *477*, 162–167. [[CrossRef](#)]
13. Kurishita, H.; Matsuo, S.; Arakawa, H.; Sakamoto, T.; Kobayashi, S.; Nakai, K.; Takida, T.; Kato, M.; Kawai, M.; Yoshida, N. Development of re-crystallized W-1.1%TiC with enhanced room-temperature ductility and radiation performance. *J. Nucl. Mater*. **2010**, *398*, 87–92. [[CrossRef](#)]
14. Du, J.; Höschel, T.; Rasinski, M.; Wurster, S.; Grosinger, W.; You, J.H. Feasibility study of a tungsten wire-reinforced tungsten matrix composite with ZrOx interfacial coatings. *Compos. Sci. Technol*. **2010**, *70*, 1482–1489. [[CrossRef](#)]
15. Du, J.; Höschel, T.; Rasinski, M.; You, J.H. Interfacial fracture behavior of tungsten wire/tungsten matrix composites with copper-coated interfaces. *Mater. Sci. Eng. A-Struct*. **2010**, *527*, 1623–1629. [[CrossRef](#)]
16. Hobe, J.; Gumbsch, P. On the potential of tungsten-vanadium composites for high temperature application with wide-range thermal operation window. *J. Nucl. Mater*. **2010**, *400*, 218–231. [[CrossRef](#)]
17. Lian, Y.Y.; Liu, X.; Feng, F.; Song, J.P.; Yan, B.Y.; Wang, Y.M.; Wang, J.B.; Chen, J.M. Mechanical properties and thermal shock performance of W-Y₂O₃ composite prepared by high-energy-rate forging. *Phys. Scr*. **2017**, *T170*, 0140440. [[CrossRef](#)]
18. Zhang, T.; Du, W.Y.; Zhan, C.Y.; Wang, M.M.; Deng, H.W.; Xie, Z.M.; Li, H. The high thermal stability induced by a synergistic effect of ZrC nanoparticles and Re solution in W matrix in hot rolled tungsten alloy. *Nucl. Eng. Technol*. **2022**. [[CrossRef](#)]
19. Zhao, B.L.; Xia, Y.P.; Zhang, L.F.; Ke, J.G.; Cheng, X.; Xie, Z.M.; Liu, R.; Miao, S.; Hao, T.; Wu, X.B.; et al. Effects of rolling reduction on microstructural evolution and mechanical properties of W-0.5 wt%ZrC alloys. *Mater. Sci. Eng. A-Struct*. **2022**, *830*, 142310. [[CrossRef](#)]
20. Shi, J.; Luo, L.M.; Wang, S.; Pan, W.Q.; Xu, Q.; Zan, X.; Zhu, X.Y.; Cheng, J.G.; Wu, Y.C. Preparation of TiC-doped W-Ti alloy and heat flux performance test under laser beam facility. *Fusion Eng. Des*. **2018**, *126*, 79–86. [[CrossRef](#)]
21. Li, L.; Fan, J.L.; Tian, L.M.; Cheng, H.C.; Zhang, H.B. Modification of the interface and its influence on the performance of W-6 wt% TiC composite. *Mater. Sci. Eng. A-Struct*. **2021**, *819*, 141442. [[CrossRef](#)]
22. Xie, Z.M.; Miao, S.; Zhang, T.; Liu, R.; Wang, X.P.; Fang, Q.F.; Hao, T.; Zhuang, Z.; Liu, C.S.; Lian, Y.Y.; et al. Recrystallization behavior and thermal shock resistance of the W-1.0 wt% TaC alloy. *J. Nucl. Mater*. **2018**, *501*, 282–292. [[CrossRef](#)]
23. Yang, J.J.; Chen, G.; Chen, Z.; Mu, X.D.; Yu, Y.; Zhang, L.; Li, X.Y.; Qu, X.H.; Qin, M.L. Effects of doping route on microstructure and mechanical properties of W–1.0wt.%La₂O₃ alloys. *T. Nonferr. Metal. Soc*. **2020**, *30*, 3296–3306. [[CrossRef](#)]
24. Zhang, J.; Luo, L.M.; Zhu, X.Y.; Chen, H.Y.; Chen, J.L.; Zan, X.; Cheng, J.G.; Wu, Y.C. Effect of doped Lu₂O₃ on the microstructures and properties of tungsten alloy prepared by spark plasma sintering. *J. Nucl. Mater*. **2015**, *456*, 316–320. [[CrossRef](#)]
25. Lv, Y.Y.; Han, Y.; Zhao, S.Q.; Du, Z.Y.; Fan, J.L. Nano-in-situ-composite ultrafine-grained W-Y₂O₃ materials: Microstructure, mechanical properties and high heat load performances. *J. Alloy. Compd*. **2021**, *855*, 157366. [[CrossRef](#)]
26. Wang, J.F.; Zuo, D.W.; Zhu, L.; Li, W.W.; Tu, Z.B.; Dai, S. Effects and influence of Y₂O₃ addition on the microstructure and mechanical properties of binderless tungsten carbide fabricated by spark plasma sintering. *Int. J. Refract. Met. Hard Mater*. **2018**, *71*, 167–174. [[CrossRef](#)]
27. Yao, G.; Liu, X.P.; Zhao, Z.H.; Luo, L.M.; Cheng, J.G.; Zan, X.; Wang, Z.M.; Xu, Q.; Wu, Y.C. Excellent performance of W-Y₂O₃ composite via powder process improvement and Y₂O₃ refinement. *Mater. Design*. **2021**, *212*, 110249. [[CrossRef](#)]
28. Tan, X.Y.; Luo, L.M.; Chen, H.Y.; Zhu, X.Y.; Zan, X.; Luo, G.N.; Chen, J.L.; Li, P.; Cheng, J.G.; Liu, D.P.; et al. Mechanical properties and microstructural change of W-Y₂O₃ alloy under helium irradiation. *Sci. Rep*. **2015**, *5*, 12755. [[CrossRef](#)]
29. Wang, K.; Ren, D.Y.; Zan, X.; Luo, L.M.; Pantleon, W.; Wu, Y.C. Evolution of microstructure and texture in a warm-rolled yttria dispersion-strengthened tungsten plate during annealing in the temperature range between 1200 degrees C and 1350 degrees C. *J. Alloy. Compd*. **2021**, *883*, 160767. [[CrossRef](#)]
30. Huber, A.; Burdakov, A.; Zlobinski, M.; Wirtz, M.; Coenen, J.W.; Linke, J.; Mertens, P.; Philipps, V.; Pintsuk, G.; Schweer, B.; et al. Investigation of the Impact on Tungsten of Transient Heat Loads Induced by Laser Irradiation, Electron Beams and Plasma Guns. *Fusion Sci. Technol*. **2013**, *63*, 197–200. [[CrossRef](#)]
31. Liu, X.; Lian, Y.Y.; Chen, L.; Chen, Z.K.; Chen, J.M.; Duan, X.R.; Fan, J.L.; Song, J.P. Experimental and numerical simulations of ELM-like transient damage behaviors to different grade tungsten and tungsten alloys. *J. Nucl. Mater*. **2015**, *463*, 166–169. [[CrossRef](#)]
32. Gao, Y.; Sun, J.L.; Yun, B. Simulative Study of Evolution Behavior of Transverse Surface Crack in Rolling Process. *Adv. Mater. Res*. **2012**, *403–408*, 88–92. [[CrossRef](#)]

33. Yao, G.; Tan, X.Y.; Luo, L.M.; Hong, K.J.; Zan, X.; Xu, Q.; Zhu, X.Y.; Lian, Y.Y.; Liu, X.; Wu, Y.C. Surface damage evolution during transient thermal shock of W-2%vol Y₂O₃ composite material in different surfaces. *Fusion Eng. Des.* **2019**, *139*, 86–95. [[CrossRef](#)]
34. Zhang, T.; Xie, Z.M.; Yang, J.F.; Hao, T.; Liu, C.S. The thermal stability of dispersion-strengthened tungsten as plasma-facing materials: A short review. *Tungsten*. **2019**, *1*, 187–197. [[CrossRef](#)]
35. Matsuda, Y.; Yamashita, S.; Miyamoto, Y.; Motoi, D.; Okita, T.; Hoashi, E.; Imano, K.; Ueda, Y. In-situ measurement of surface modifications of tungsten exposed to pulsed high heat flux for divertor design in tokamak-type fusion nuclear reactors. *Fusion Eng. Des.* **2020**, *161*, 112042. [[CrossRef](#)]
36. Okita, T.; Matsuda, Y.; Saito, S.; Hoashi, E.; Imano, K.; Ueda, Y. Observation of surface deformation of tungsten exposed to single pulsed high heat flux and magnetic field for divertor design. *Fusion Eng. Des.* **2021**, *171*, 112547. [[CrossRef](#)]
37. Farid, N.; Zhao, D.; Oderji, H.Y.; Ding, H. Cracking and damage behavior of tungsten under ELM's like energy loads using millisecond laser pulses. *J. Nucl. Mater.* **2015**, *463*, 241–245. [[CrossRef](#)]
38. Bazylev, B.; Janeschitz, G.; Landman, I.; Loarte, A.; Klimov, N.S.; Podkovyrov, V.L.; Safronov, V.M. Experimental and theoretical investigation of droplet emission from tungsten melt layer. *Fusion Eng. Des.* **2009**, *84*, 441–445. [[CrossRef](#)]
39. Uytendhouwen, I.; Decret, M.; Hirai, T.; Linke, J.; Pintsuk, G.; Van Oost, G. Influence of recrystallization on thermal shock resistance of various tungsten grades. *J. Nucl. Mater.* **2007**, *363*, 1099–1103. [[CrossRef](#)]
40. Pintsuk, G.; Uytendhouwen, I. Thermo-mechanical and thermal shock characterization of potassium doped tungsten. *Int. J. Refract. Met. Hard Mater.* **2010**, *28*, 661–668. [[CrossRef](#)]